Renewable Energy 122 (2018) 55–64

Contents lists available at ScienceDirect

Renewable Energy

journal homepage: www.elsevier.com/locate/renene

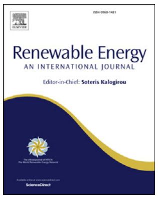

Quantifying thermal decomposition regimes of textile dyeing sludge, pomelo peel, and their blends

Candie Xie [a], Jingyong Liu [a, *], Wuming Xie [a], Jiahong Kuo [a], Xingwen Lu [a], Xiaochun Zhang [a], Yao He [a], Jian Sun [a], Kenlin Chang [a, b], Wenhao Xie [a], Chao Liu [a], Shuiyu Sun [a], Musa Buyukada [c], Fatih Evrendilek [c]

[a] *School of Environmental Science and Engineering, Institute of Environmental-Health and Pollution Control, Guangdong University of Technology, Guangzhou 510006, China*
[b] *Institute of Environmental Engineering, National Sun Yat-Sen University, Kaohsiung 80424, Taiwan, ROC*
[c] *Department of Environmental Engineering, Abant Izzet Baysal University, Bolu, 14052, Turkey*

ARTICLE INFO

Article history:
Received 5 August 2017
Received in revised form
27 December 2017
Accepted 23 January 2018
Available online 2 February 2018

Keywords:
Textile dyeing sludge
Pomelo peel
Co-combustion
TG-FTIR
Thermal decomposition behaviors

ABSTRACT

Thermal decomposition behaviors of textile dyeing sludge (TDS), pomelo peel (PP), and their blends (TP) were detected using TG-FTIR. The blend ratios of TDS to PP ranged from 10 to 40 wt% and were subjected to heat above room temperature up to 1000 °C under four heating rates. Our results pointed to four stages for TDS combustion and three stages for PP combustion. The interactions between TDS and PP exerted inhibitive effects during the co-combustion process. Releases of CO_2 and light organics occurred less with a TP ratio of 70%–30% (TP73) than with the individual fuels. Apparent activation energy (E_a) was obtained using Flynn-Wall-Ozawa (FWO) and Kissinger-Akahira-Sunose (KAS) methods. The FWO-based E_a estimates were in the range of 59.7–122.2 $kJ \cdot mol^{-1}$ for TDS, 84.4–243.5 $kJ \cdot mol^{-1}$ for PP, and 94.3–142.1 $kJ \cdot mol^{-1}$ for TP73.

© 2018 Elsevier Ltd. All rights reserved.

1. Introduction

Textile printing and dyeing industries are among the most heavily polluting sectors that not only require large quantities of freshwater but also generate large volumes of wastewater and sludge after the treatment. The total amount of wastewater from textile printing and dyeing industries in China reached about 2.15 billion tons (t), with the resultant generation of textile dyeing sludge (TDS) of 5.38 million t (including 80% water content) [1]. Given rapidly growing rates of TDS, its high toxicity and low degradability, and limitations of the conventional disposal technologies such as landfill, sea disposal, and fertilizers, there is an urgent need to develop environmentally and economically effective ways of its disposal [2–5]. Sludge (co-)combustion appears to be a promising way to maximize sludge reduction [6]. For example, most European Union countries have promoted sludge (co-)combustion and incineration as the mainstream treatment technology for TDS [7]. However, as the mono-combustion of TDS is unstable and incomplete due to its high ash content and low calorific value [8], seeking co-combustion alternatives for TDS is of pivotal significance to minimization of environmental issues and maximization of useful energy.

Thermogravimetry (TG) analysis used to explore thermal regimes and reaction kinetics of mono- and co-combustions of sludge, coal, and biomass under different conditions showed that co-combustion performance of sludge improved significantly with the concurrent use of biomass [9–11]. For example, Font et al. [12] quantified TG curves of two sludge types at different heating rates, proposing a kinetic model with three independent but parallel reactions. Liu et al. [13] explored combustion regimes of different sludge sources and their physicochemical properties. The blend of coal and sludge (50 wt%) was reported to show reactivity similar to that of sludge in the low temperature region (<350 °C) and similar to that of coal in the high temperature region (>350 °C) [14]. The combustion regimes of miscanthus, poplar wood, and rice husk were found to increase ignition and burnout temperatures with the increased heating rate [15]. Wang et al. [16] determined significant synergistic effects during the co-pyrolysis of sewage sludge and

---

* Corresponding author. Tel : +86 020 39322291 ; fax : +86 020 39322548.
E-mail addresses: www053991@126.com, Liujy@gdut.edu.cn (J. Liu).

https://doi.org/10.1016/j.renene.2018.01.093
0960-1481/© 2018 Elsevier Ltd. All rights reserved.

straw. The synergistic effect of the TDS and microalgae co-combustion was reported to improve both char catalytic effect and alkali metal melting-induced effect [8]. Deng et al. [17] related the interaction effect of oil sludge and wood primarily to co-combustion temperature.

Over 2 million t pomelos, a characteristic fruit of China, are produced annually with the generation of a large amount of pomelo peel (PP) as a byproduct [18]. Thus far, PP has been used to extract pectin, flavonoids, essential oils, natural pigments, a variety of other active ingredients, and biosorbents [19–22]. However, the present utilization of these value-added byproducts is very limited and massive amounts of PP are frequently dumped in garbage. In line with the sludge treatment and disposal policies of China, the co-combustion of garbage and sludge is highly encouraged. PP is rich in organic matter, cellulose and lignin [18]; however, it has never been used as a potential biofuel source in a (co-)combustion process for energy utilization. Instead, thermal decomposition behaviors of TDS and orange peels were quantified combining TG analyzer-Fourier transform infrared spectroscopy (TG-FTIR) techniques, with no report on the analysis of evolved gas [23,24]. However, it is necessary to probe variations in gaseous products during the co-combustion process in order to predict the possible differences among thermal decomposition behaviors of blended versus individual samples. There exists a knowledge gap as to the quantification and understanding of the potential co-combustion of PP and TDS, and the shortcomings of mono-combustion of TDS.

The objectives of the present study were to (1) explore thermal decomposition regimes of TDS and PP co-combustion using the combined TG-FTIR technique under the air atmosphere (composed of 21% O_2 and 79% N_2), (2) compute various characteristic combustion indices to evaluate impact of PP on the combustion characteristics of TDS under four heating rates and four blend ratios, and (3) quantify kinetics and evolution of gaseous products during (co-)combustion of PP and TDS. The Flynn-Wall-Ozawa (FWO) and Kissinger-Akahira-Sunose (KAS) iso-conversional methods were applied in the kinetic analysis to estimate apparent activation energy (E_a).

2. Methods

2.1. Sample preparation

The block-shaped TDS used in this study was obtained from a textile printing and dyeing plant from Dongguan in the Guangdong Province, China. Pomelo peel was collected from a fruit market of Guangzhou University Mega Center. After being milled and sieved into particles of 74 μm diameter, TDS and PP samples were dried in the oven at 105 °C for 24 h. The TDS and PP samples were blended with the following PP weight (wt) percentages of 10%, 20%, 30% and 40% coded as TP91, TP82, TP73 and TP64, respectively.

2.2. TG-FTIR experiments

The (co-)combustion characteristics of TDS and PP were analyzed using a TG analyzer system (NETZSCH STA 409 PC Luxx, Germany) coupled with a FTIR spectrometer (TENSOR 27 FTIR, Germany). The transfer line and gas cell of the FTIR spectrometer were heated at 200 °C to prevent the condensation of evolved gases. FTIR spectra from 4000 to 650 cm^{-1} were recorded at a resolution of 4 cm^{-1}. The test data were processed using the OMNIC software (Thermo Electron, USA).

In the TG experiments, all the samples (10 ± 0.5 mg) were heated at temperatures up to 1000 °C using the four heating rates of 15, 20, 25 and 30 $°C \cdot min^{-1}$ under the air atmospheric condition composed of 21% O_2 and 79% N_2, at a flow rate of 50 $mL \cdot min^{-1}$. Each test was conducted three times to ensure reproducibility, accuracy, and that errors of results were within ±2%.

2.3. Mineral composition of samples

Mineral compositions of the individual fuels were characterized using an energy dispersive X-ray fluorescence spectrometer (EDX-7000, SHIMADZU, Japan).

2.4. Performance index

For an integrative evaluation of the (co-)combustion characteristics of TDS and PP, the comprehensive combustion index (S) was used and was defined as follows [25]:

$$S = \frac{(dW/dt)_{\max}(dW/dt)_{mean}}{T_i^2 T_f} \tag{1}$$

where $(dW/dt)_{\max}$ is the maximum mass loss rate, while $(dW/dt)_{mean}$ is the average mass loss rate ($\% \cdot min^{-1}$). The higher the S values are, the better the combustion properties of the samples are.

2.5. Interaction indices

In order to confirm the possible existence of interaction effects (accelerative or inhibitive) between TDS and PP during the co-combustion, the TG curves were obtained from the mass loss of the individual samples which were in contrast to the experimental values. The estimated TG (TG_{cal}) values for the TP blends were defined as follows [9]:

$$TG_{cal} = \gamma_{TDS} TG_{TDS} + \gamma_{PP} TG_{PP} \tag{2}$$

where γ_{TDS} and γ_{PP} were the mass fractions of TDS and PP in the blends, respectively, while TG_{TDS} and TG_{PP} were the corresponding weight losses of the individual samples.

To gain further insight into the degree and variation of the interaction effects on the co-combustion, deviations from the TG_{cal} values were introduced using the following equation [26]:

$$Deviation(\%) = \left[\frac{TG_{\exp} - TG_{cal}}{TG_{cal}}\right] \times 100\% \tag{3}$$

2.6. Kinetics

According to the Arrhenius equation, the general kinetic equation for the solid-state thermal transformation can be expressed thus:

$$\frac{d\alpha}{dt} = \beta \frac{d\alpha}{dT} = f(\alpha)k(T) = A \exp\left(-\frac{E_a}{RT}\right) f(\alpha) \tag{4}$$

where α is the degree of conversion for the solid reactant; $k(T)$ is the constant of reaction rate; $f(\alpha)$ is the reaction model of the thermodynamic mechanism; A (min^{-1}) is the apparent pre-exponential factor; E_a ($J \cdot mol^{-1}$) is activation energy; R is the universal gas constant ($8.314\ J \cdot mol^{-1} \cdot K^{-1}$); T (K) is the absolute temperature; t (min) is the reaction time; and β ($°C \cdot min^{-1}$) is the heating rate.

The mass loss fraction was estimated from the corresponding TG curves and defined as follows:

$$\alpha = \frac{m_0 - m_t}{m_0 - m_f} \tag{5}$$

where m_0 and m_f are sample masses at the initial and end of the reactions, respectively, and m_t refers to sample mass at time t during the (co-)combustion process.

The integration form of the Eq. (4) can be expressed thus:

$$g(\alpha) = \int_0^{\alpha} \frac{d\alpha}{f(\alpha)} = \frac{A}{\beta}\int_0^{T} \exp\left(-\frac{E_a}{RT}\right) dT = \frac{AE_a}{\beta R}\int_x^{\infty} \frac{\exp(-x)}{x^2} dx = \frac{AE_a}{\beta R} p(x) \tag{6}$$

where $g(\alpha)$ is the integral function of conversion, $x = E_a/RT$, and $p(x)$ is a temperature integration function with no exact solution.

The iso-conversional method is used to estimate the activation energy independent of the reaction mechanism, with no need to presume the analytical form of $f(\alpha)$ function [27]. In this study, E_a was estimated using the iso-conversional methods of FWO and KAS. The FWO method is based on Doyle's approximation yields using the below equation [28]:

$$\log \beta = \log\left(\frac{AE_a}{Rg(\alpha)}\right) - 2.315 - 0.4567\frac{E_a}{RT} \tag{7}$$

where E_a depending on the conversion degree can be estimated from the slope of $\log \beta$ versus $1/T$ ($-0.4567\ E_a/R$).

The KAS method is derived from the Coats-Redfern approximation of $p(x) = x^{-2}e^{-x}$ as follows [29]:

$$\ln\left(\frac{\beta}{T^2}\right) = \ln\left(\frac{AR}{E_a g(\alpha)}\right) - \frac{E_a}{RT} \tag{8}$$

where the term of $\ln(\beta/T^2)$ versus $1/T$ at a slope $-E_a/R$ can be used to determine E_a.

3. Result and discussion

3.1. Physicochemical properties of individual samples

Physicochemical properties of TDS, PP and other biomass materials reported in related literature including straw (ST), wheat straw (WS), orange peel (OP), babool seeds (BS) and water hyacinth (WH) were compared in Table 1. As can be seen from Table 1, PP had relatively higher volatile matter (68.04%) and lower ash content (2.06%) than did the reported biomass materials. In addition, PP had a relatively high carbon content (42.40%) and lower heating value (16.82 MJ·kg^{-1}). All these properties pointed to PP as a feasible alternative fuel for energy production [33]. Also, the lower sulfur and nitrogen contents of PP were reflected as the lower emissions of noxious gases during the PP combustion. The above indicators discussed confirmed that the mono-combustion of TDS was unstable and incomplete, and that the co-combustion of TDS and PP was feasible.

3.2. Individual combustion processes of TDS and PP

As shown in Fig. 1, the combustion process of TDS was divided into the four stages. The first stage occurred between 28 and 208 °C mostly as a result of moisture evaporation, leading to a weight loss by 11.25% in Table 1. The degradations of free and bound water, and some light organic compounds also occurred in this stage. The second stage between 208 and 675 °C mainly resulted from the release of volatile matters and the decomposition of macromolecule organic matters such as fiber, proteins, and saturated aliphatic chains [34]. There were primarily two types of organic volatile compounds in TDS corresponding to the two weight loss peaks of the derivative thermogravimetry (DTG) curve at 329.9 °C and 452.2 °C, respectively. In particular, the maximum weight loss occurred at 329.9 °C. A clear side peak appeared when the temperature was above 500 °C which may be attributed to the different bond strengths due to the release of the organic matter, thus resulting in different combustibility of the volatiles. This stage as the main decomposition process of TDS accounted for about 45.97% of the total weight loss. The third stage between 675 and 850 °C was the carbonization process due to the combustion of fixed carbon and organic matters that were difficult to degrade, by a weight loss of 3.18%. The fourth stage between 850 and 1000 °C was related to the decomposition of inorganic minerals such as calcium carbonate, dolomite, and kaolin [8], by a slight weight loss of 2.03%.

The TG-DTG curve of PP significantly differed from that of TDS in terms of the combustion regime at the heating rate of 20 °C·min^{-1} (Fig. 1). The following three main stages were captured during the thermal decomposition of PP: the evaporation of moisture between 28 and 150 °C; the release and combustion of volatiles between 150 and 410 °C; and decomposition of carbonaceous residues between 410 and 480 °C. About 4% weight loss in the first stage occurred primarily due to the release of bound water from PP. The second stage constituted the major period of the combustion process of PP with about 72.77% weight loss primarily due to the decomposition of hemicellulose, cellulose, and lignin. Due to its higher activity than cellulose and lignin in thermal decomposition [35], decomposition of hemicellulose initially took place in the temperature

Table 1
Ultimate and proximate analyses of textile dyeing sludge (TDS), pomelo peel (PP) and other biomass materials reported in related literature on an air-dried basis.

Analysis	TDS	PP	ST [30]	WS [16]	OP [31]	BS [11]	WH [9]
Ultimate analysis (wt%)							
Carbon	20.20	42.40	45.80	43.92	39.71	54.10	38.96
Hydrogen	6.08	6.31	5.96	4.47	6.20	6.12	5.30
Oxygen[a]	20.00	35.06	40.00	40.98	53.03	34.53	35.18
Nitrogen	3.22	0.59	0.45	0.44	0.46	5.23	3.51
Sulfur	2.76	0.01	0.16	0.30	0.60	–	0.27
Proximate analysis (wt%)							
Moisture content	11.70	13.57	10.30	3.88	9.20	12.50	8.32
Volatile matters	44.71	68.04	69.70	72.10	–	69.10	61.57
Ash content	36.04	2.06	4.20	6.01	2.94	7.30	8.67
Fixed carbon	7.55	16.33	15.80	18.01	13.07	11.00	21.44
LHV[b] (MJ·kg^{-1})	9.87	16.82	17.41	14.77	–	–	13.51

[a] O, calculated by O = 100%–C–H–N–S–M–A [32].
[b] LHV, lower heating value on a dry weight basis.

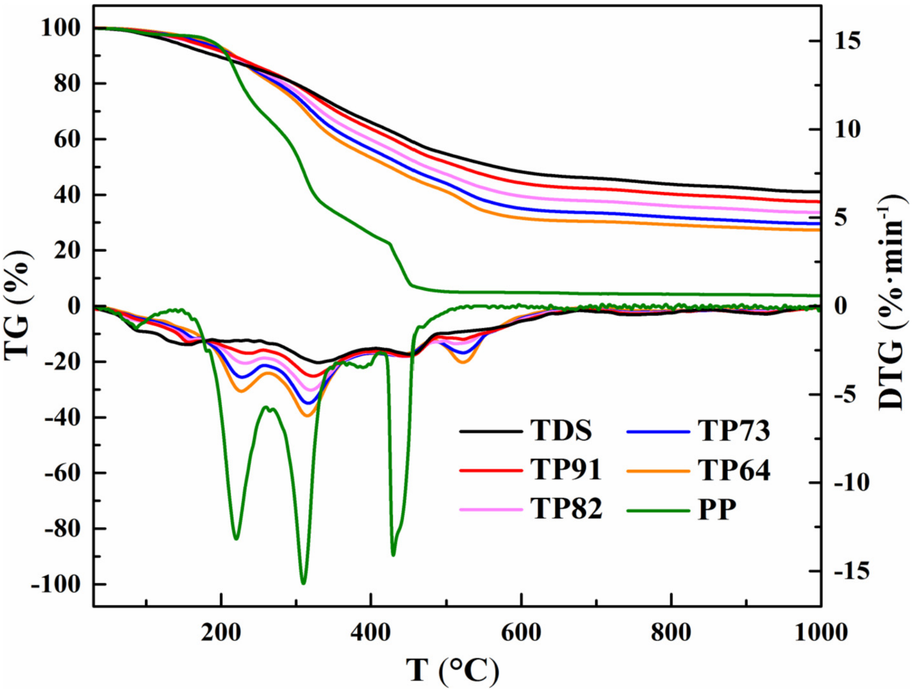

Fig. 1. TG-DTG curves in air (21%O_2+79%N_2) atmosphere at a heating rate of 20 °C·min^{-1}.

range of 220–315 °C which was followed by decomposition of cellulose in the temperature range of about 315–400 °C. However, the thermal degradation of lignin occurred at a wider temperature range of 180–900 °C [36]. The weight loss at the third stage elucidated 18.84% of the total weight loss primarily due to the carbonization of cellulose and lignin. In this stage during which most volatiles of PP were reduced, oxygen was diffused gradually to the surface of carbon fixed by the pore structure, thus facilitating the burning of fixed carbon [37]. The major reaction phase of PP occurred in the temperature range of 180–480 °C, with the three distinct shoulder peaks of the DTG curve corresponding to 220, 309, and 430 °C, respectively. The weight loss peak occurred at 309 °C and was caused by the decomposition of large amounts of cellulose and lignin.

Given the final residual masses of TDS (41.06%) and PP (3.68%), we can infer that the combustion of PP was more intense and thorough than that of TDS. A comparison of the DTG curves in Fig. 1 pointed to the three peaks during the major reaction phase of PP and to only the two peaks for TDS between 180 and 480 °C. The maximum mass loss rate of PP was higher than that of TDS, whereas the weight loss peaks of PP spanned a narrower temperature range than those of TDS. This indicated the more concentrated and intense releases of volatiles from the combustion of PP because PP contained a large amount of hemicellulose, cellulose, other combustible components, high organic matter content, and low ash content [18]. Ignition temperature (T_i) defined as the temperature at which a sample starts to be burnt and determined by the TG-DTG tangent method [38] was estimated at 248.1 °C for TDS and 197.3 °C for PP (Table 2). Burnout temperature (T_f) defined as the temperature at which 98% conversion (α) is achieved at the end of the reaction [39] was determined as 907.1 °C for TDS and 481.9 °C for PP (Table 2). These results showed that PP had a more easily degradable structure with a higher volatile content, while TDS had a higher ash content. Thus, higher energy requirement by the rupture of chemical bonds in TDS necessitated the occurrence of higher temperatures [23]. These results are consistent with the analyses shown in Table 1.

Table 2
Characteristic parameters of all the individual fuels and their blends used in this study and other biomass materials reported in related literature in air atmosphere (21% O_2+79% N_2) at a heating rate of 20 °C·min^{-1}.

Samples	T_i^a (°C)	T_m^b (°C)	DTG^c_{max} (%·min^{-1})	T_f^d (°C)	M_f^e (%)	S^f (10^{-7})
TDS	248.1	329.9	3.20	907.1	41.06	0.731
TP91	207.9	323.2	3.96	905.9	37.50	1.367
TP82	204.7	319.7	4.76	879.2	33.63	1.853
TP73	202.8	316.7	5.50	865.4	29.60	2.356
TP64	200.9	315.1	6.21	838.8	27.30	2.893
PP	197.3	309.9	15.72	481.9	3.68	18.010
SP [40]	299.2	345.0	25.60	526.5	–	8.490
ES [40]	295.5	337.5	22.90	527.7	–	7.370
WH [9]	258.5	289.2	16.57	959.9	6.55	14.360
MA [23]	251.6	336.0	8.58	786.1	23.17	–
RS [41]	271.0	304.0	15.38	508.0	16.61	7.377

T_i^a, ignition temperature; T_m^b, peak temperature; DTG^c_{max}, maximum mass loss rate; T_f^d, burnout temperature; M_f^e, residual mass; S^f, comprehensive combustion index expressed in $\%^2\cdot{}^\circ C^{-3}\cdot min^{-2}$.

Give the characteristic parameters reported in Table 2, PP had a relatively lower ignition temperature (197.3 °C) and residual mass (3.68%) than did stone pine (SP), eucalyptus (ES), water hyacinth (WH), microalgae (MA) and rice straw (RS). This indicated better ignition and burnout properties of PP. PP also had a better comprehensive combustion performance ($18.010 \times 10^{-7}\%^2\cdot{}^\circ C^{-3}\cdot min^{-2}$). Therefore, these characteristics further confirmed that PP would be valuable to the thermal process and energy utilization.

3.3. *Co-combustion processes of TDS and PP*

The characteristic co-combustion parameters of the TP blends are presented in Table 2. The TG-DTG profiles of the blends in response to the increased PP ratio under the heating rate of 20 °C·min^{-1} are shown in Fig. 1. When the individual reactions and blend interactions were compared, the blends showed the three regions of reactivity. The reactivity of the blends was similar to that of TDS in the temperature regions of about 28–180 °C and 560–1000 °C and to that of PP in its major reaction phase between 180 and 560 °C. Between 180 and 560 °C, a significant trend of weight loss occurred in the TG curves corresponding to the four distinct peaks of the DTG curves. The maximum weight loss rate (DTG_{max}) increased with the increased PP. DTG_{max} values of the blends varied between those of TDS ($3.20\%\cdot min^{-1}$) and PP ($15.72\%\cdot min^{-1}$), thus indicating a higher PP proportion and a higher DTG_{max} for the blends. This case is probably associated with the enhanced release of volatile substances [42]. PP required a lower temperature than did TDS to release their volatiles, and thus, PP was burnt quickly and intensively during the entire temperature range due to their higher volatiles content and weaker bonds [43]. Above 560 °C, the reactivity of the blends changed from that of PP to that of TDS gradually due to the lower degradability of TDS than PP. The striking difference in the trend at the end of the TG curves is mostly likely to stem from the difference in ash content between TDS and PP (Table 1). Therefore, a decrease in residual mass as a result of the blends with a higher ratio of PP would be expected during the co-combustion [44].

From Fig. 2(a)–(e), the (non-)linear trends in T_i, T_f, T_m, DTG_{max} and M_f were elucidated as a function of the TP fractions (10–40%). Their coefficients of determination (R^2) range from 0.9859 to 0.9993. The trends of changes in T_f and DTG_{max} were linear, whereas those of T_i, T_m and M_f had an exponential relationship. With the increased PP, T_i, T_f, T_m and M_f decreased, whereas DTG_{max} increased. T_i values of TP varied between those of TDS and PP. Moreover, T_i values of the blends were estimated at 207.9 °C for TP91, 204.7 °C for TP82, 202.8 °C for TP73 and 200.9 °C for TP64 and were less than those of TDS. This implied that more organics were quickly released and volatilized with PP than with TDS. The ascending PP proportion (10–40%) of the blends led to the decreases in T_m (323.2–315.1 °C), T_f (905.9–838.8 °C) and M_f (37.50–27.30%). On the contrary, the intensity of the maximum weight loss peak increased from $3.96\%\cdot min^{-1}$ to $6.21\%\cdot min^{-1}$. This was consistent with the following inference that the higher the PP content was, the larger the weight loss occurred, and the higher the reactivity of the blends was [45]. All the parameters of the blends were improved relative to the mono-combustion of TDS, suggesting that the addition of PP served to improve the combustion performance of TDS.

As shown in Fig. 2(f), the S index value changed linearly with the increased TP ($S = 0.5081x + 0.847$, $R^2 = 0.9995$). S value of PP was estimated at $18.010 \times 10^{-7}\%^2\cdot °C^{-3}\cdot min^{-2}$, over one order of magnitude larger than that of TDS ($0.731 \times 10^{-7}\%^2\cdot °C^{-3}\cdot min^{-2}$), while S value of TP ($1.367–2.893 \times 10^{-7}\%^2\cdot °C^{-3}\cdot min^{-2}$) fell in between the two individual samples. In conclusion, the addition of a

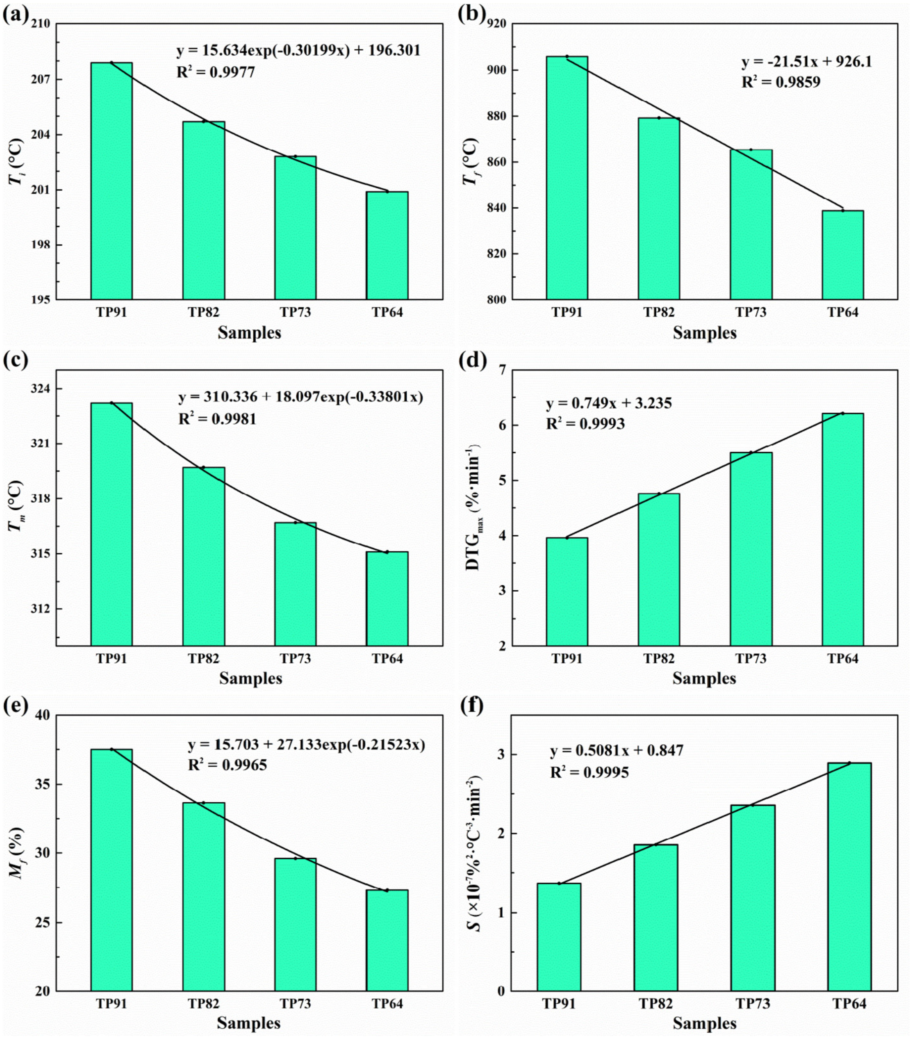

Fig. 2. Relationships of (a) T_i, (b) T_f, (c) T_m, (d) DTG_{max}, (e) M_f and (f) S to TP blends (10–40 wt%).

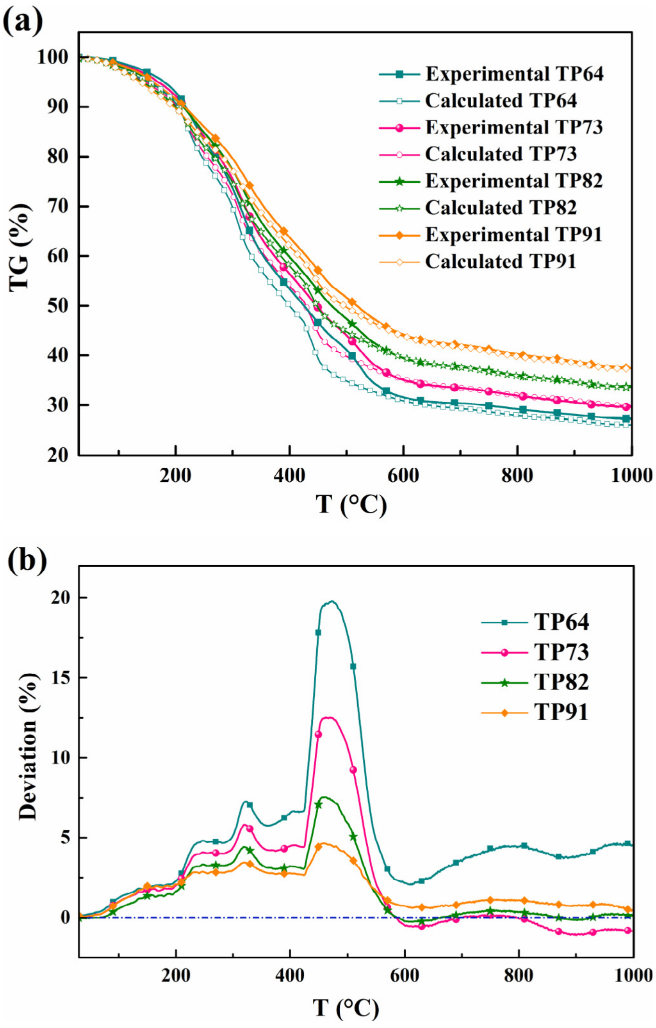

Fig. 3. Comparison of experimental versus estimated TG curves of the four blends for (a) deviation profiles and (b) as a function of temperature.

suitable amount of PP to TDS could offset the deficiencies mutually, thus improving the combustion performance of TDS.

3.4. Interactions between TDS and PP

As was shown in Fig. 3(a), the values of TG_{exp} and TG_{cal} at $\beta = 20\,^{\circ}\mathrm{C}\cdot\mathrm{min}^{-1}$ indicated that TG_{cal} mostly lagged behind TG_{exp} at any TP type with each of which their curves differed significantly. Hence, the interactions between TDS and PP exerted inhibitive instead of accelerative influences on the co-combustion process. Fig. 3(a) exhibited the two profiles. TP began to diverge initially with a slight deviation below 200 °C and then with a fast pace by about 460 °C. Finally, the divergence slowed down with the two curves converging gradually at above 460 °C. Additionally, the reaction rate of the experimental TG curve was slower than that of the calculated TG curve for TP. This might be attributed to the fact that the blends had higher volatiles than did TDS. There was more oxygen initially reacted with PP which in turn delayed the oxidation reaction of TDS. The lack of oxygen was reported to retard the decomposition rate of TP [46].

Fig. 3(b) showed the deviation curves for the co-combustion as a function of temperature. Our results suggested that the deviation was less than 2.5% below 200 °C for TP, which value was lower than the statistical significance (5%). This indicated no interactions in the blends. The reason might be the ignition temperatures of the blends above 200 °C, and occurrence of no thermal decomposition at this phase [47]. It underwent an abrupt increase at about 425 °C and reached its maximum value at around 460 °C, thus indicating the significant dominance of the inhibition at this stage. The deviation values increased with the increased TP which could be ascribed to sticky bio-oils generated from the PP combustion. A similar finding was reported for citrus dry peel during the thermal decomposition process [31]. The resultant bio-oils were most likely to coat surface of TDS particles, thus preventing the release of its volatiles. PP and TDS particles were also reported to influence the processes of thermal transmission and mass transfer [23]. As the temperature exceeded 460 °C, the PP combustion reaction gradually ceased, and thus, the inhibiting effect disappeared. Eventually at 1000 °C, the deviation values reached 0.48, 0.15, −0.83 and 4.58% corresponding to TP91, TP82, TP73 and TP64, respectively. In this stage, the inhibition process of the co-combustion was attributed to the presence of residues, chars, and ash products accumulated on the surface of TDS [46]. In addition, the inhibition of TP73 was relatively weak, and the promoting effect occurred at the deviation value < 0.

To further analyze effects of minerals on combustion, the mineral compositions of the pure samples were determined using the X-ray Fluorescence (XRF) technique. The mineral compositions of the biomass such as alkali metals (Na, and K) and alkali earth metals (Mg, and Ca) are generally considered to promote catalytic activity in the co-combustion process of fuels [48]. As shown in Table 3, the alkali and alkali earth metal contents of PP was 94.86 wt%. The high Ca (72.11 wt%) and K (21.47 wt%) contents of PP suggested its potential of improving the co-combustion performance. However, the alkali metals were reported to be inactivated by reactions with aluminosilicate minerals of fuels to form inactive alkali aluminosilicates, and thus, their catalytic effects were weakened [49]. The high Al (60.12 wt%) and Si (9.12 wt%) contents of TDS were also observed (Table 3). This suggested that the accelerative effect of alkali metals for the TP blends was hindered. Besides, aluminosilicate minerals were reacted with K, as was observed for PP, to form the low-temperature sticky melts of aluminosilicate eutectics which meant that the agglomeration and clinkering of TP blends may occur [50]. This had an inhibitive effect on the co-combustion process. Therefore, the interactions between TDS and PP turned out to be inhibitive due to the higher TDS content of the TP blends.

3.5. Effect of heating rate

The TG-DTG profiles of TP73 under the four heating rates (15, 20, 25 and 30 °C·min^{-1}) were demonstrated in Fig. 4, with their characteristic parameters in Table 4. Obviously, the TG profiles

Table 3
Mineral compositions of textile dyeing sludge (TDS) and pomelo peel (PP) (wt%).

Elements	TDS	PP
K	0.69	21.47
Ca	3.32	72.11
Mg	-	1.28
Al	60.12	-
Zn	2.15	0.47
Fe	6.81	1.31
Si	9.12	0.49
S	6.21	1.45
P	4.47	0.77
Cu	0.29	0.16
Cr	3.98	-
Ni	0.78	0.02
Ti	0.68	0.11
Others	1.38	0.36

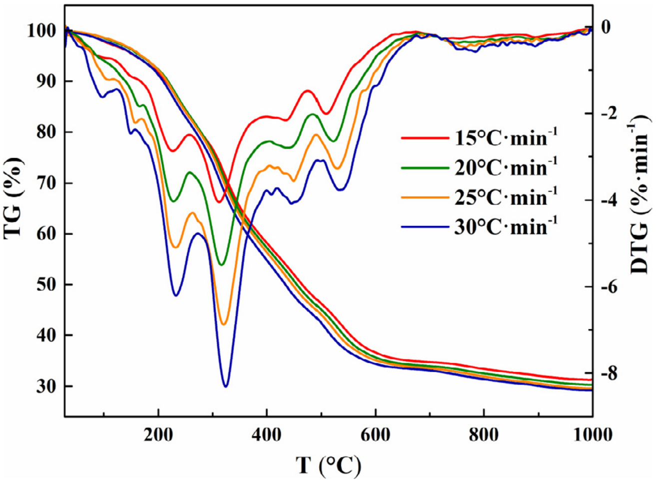

Fig. 4. TG-DTG curves for TP73 under air (21% O_2+79% N_2) atmosphere with the four heating rates.

shifted toward the low temperature range as the heating rate increased, with the weight loss peaks of the DTG profiles showing the same trends. The higher heating rates brought about the higher peaks. This resulted from the fact that the significant weight loss regions were obtained since each individual component had enough time to react under the low heating rates. At the high heating rates, reactions were virtually simultaneous, and the weight loss peaks were overlapped for the component with the adjacent combustion regions and merged to form the broader and clearer peaks [28]. The increase in the heating rate (15–30 °C·min^{-1}) in TP73 increased T_i (199.7–206.5 °C) and T_m (312.3–324.2 °C) (Table 4). Conversely, t_p (the time corresponding to DTG_{max}) and t_f (the burnout time) decreased from 19.3 to 10.3 min and from 55.71 to 27.69 min, respectively. This was because the increasing heating rate influenced the heat transfer temperature gradients between the surface and center of the samples. The heat transfer was less effective at the higher heating rates which caused a distinct lag with the increased heating rate [47].

Table 4
Characteristic parameters for TP73 under air (21% O_2+79% N_2) atmosphere with four heating rates.

Heating rates (β, °C·min^{-1})	15	20	25	30
Ignition temperature (T_i, °C)	199.7	202.8	204.6	206.5
Peak temperature (T_m, °C)	312.3	316.7	320.2	324.2
Burnout time (t_f, min)	55.71	42.1	33.41	27.69
Time corresponding to DTG_{max} (t_p, min)	19.3	14.8	12.1	10.3

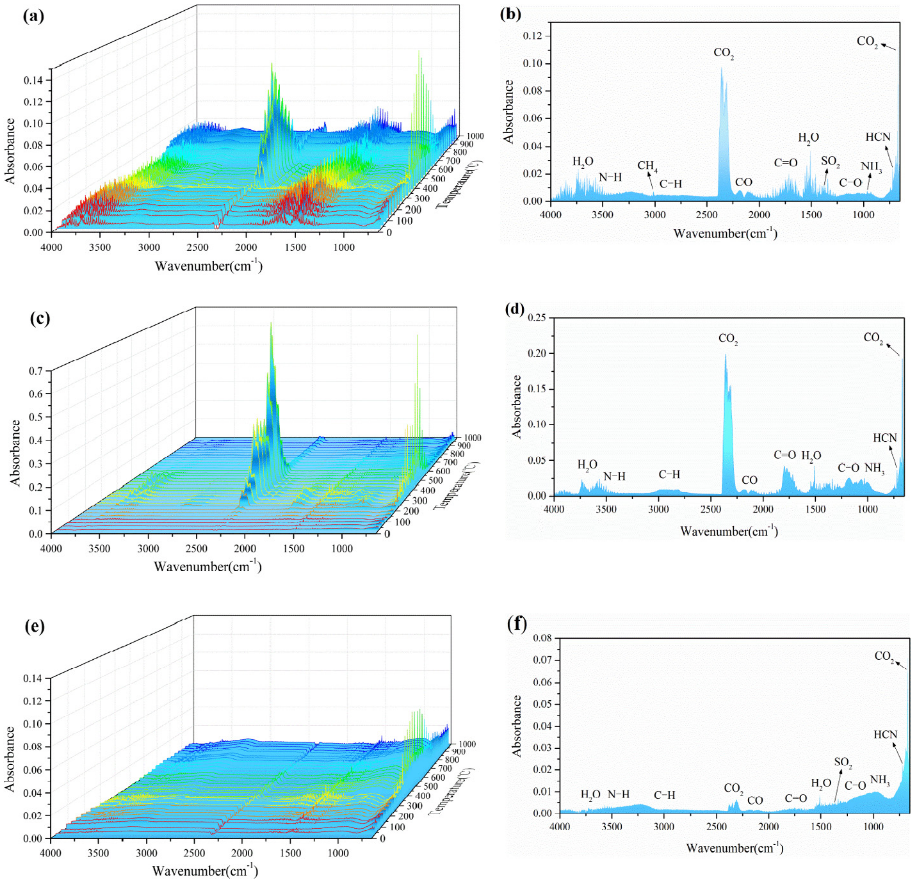

Fig. 5. Three-dimensional FTIR spectrograms of gaseous products from thermal degradation processes of (a, b) TDS, (c, d) PP and (e, f) TP73.

Table 5
A summary for FTIR bands selected for analysis of main gaseous products and functional groups in (co-)combustion.

Assignment	Wavenumber
H_2O	4000-3500, 1900-1300
CH_4	3016
CO_2	2400-2240, 780-560
CO	2240–2060
SO_2	1374
NH_3	966
HCN	714
O–H stretching vibration	4000–3500
N–H stretching vibration	3474
C–H stretching vibration	3100–2850
C=O stretching vibration	1850–1600
C–O stretching vibration	1300–950
S=O stretching vibration	1420–1300

3.6. TG-FTIR analysis of evolved gases

Fig. 5 showed the 3-D FTIR spectrograms of gaseous products from the thermal degradation process of TDS, PP and TP73, as well as their FTIR spectra at the representative temperatures. The FTIR bands of some gaseous products and functional groups during the thermal degradation process (Table 5) were collected in accordance with the FTIR characteristic absorption bands of similar samples reported in related literature [51,52]. The correspondences between the absorption peaks and the wavenumbers of the different bands or functional groups for all the samples are presented in Fig. 5(b), (d) and (f). In the case of TDS (Fig. 5(b)), the large peaks with the bands of 780–560 cm^{-1} to 2400-2240 cm^{-1} and 1900-1300 cm^{-1} to 4000-3500 cm^{-1} indicated the releases of CO_2 and H_2O, respectively, mainly due to the decomposition of organic acids, saccharides and carbonates for inorganics. The band of 3100 to 2850 cm^{-1} was assigned to the stretching of C–H bond. In particular, the band of 3016 cm^{-1} indicated the presence of methane (CH_4) due to the breakdown of methoxyl and methylene. The small peaks of 2240 to 2060 cm^{-1} were due to the generation of CO mainly from the Boudouard reaction ($C + CO_2 \leftrightarrow CO$). The S=O stretching bands occurred in the range of 1420 to 1300 cm^{-1}. The band of 1374 cm^{-1} was most likely the characteristic peak of SO_2 due to the decomposition of sulfur dyes in TDS. The other volatiles such as NH_3 at 966 cm^{-1} and HCN at 714 cm^{-1} were also detected

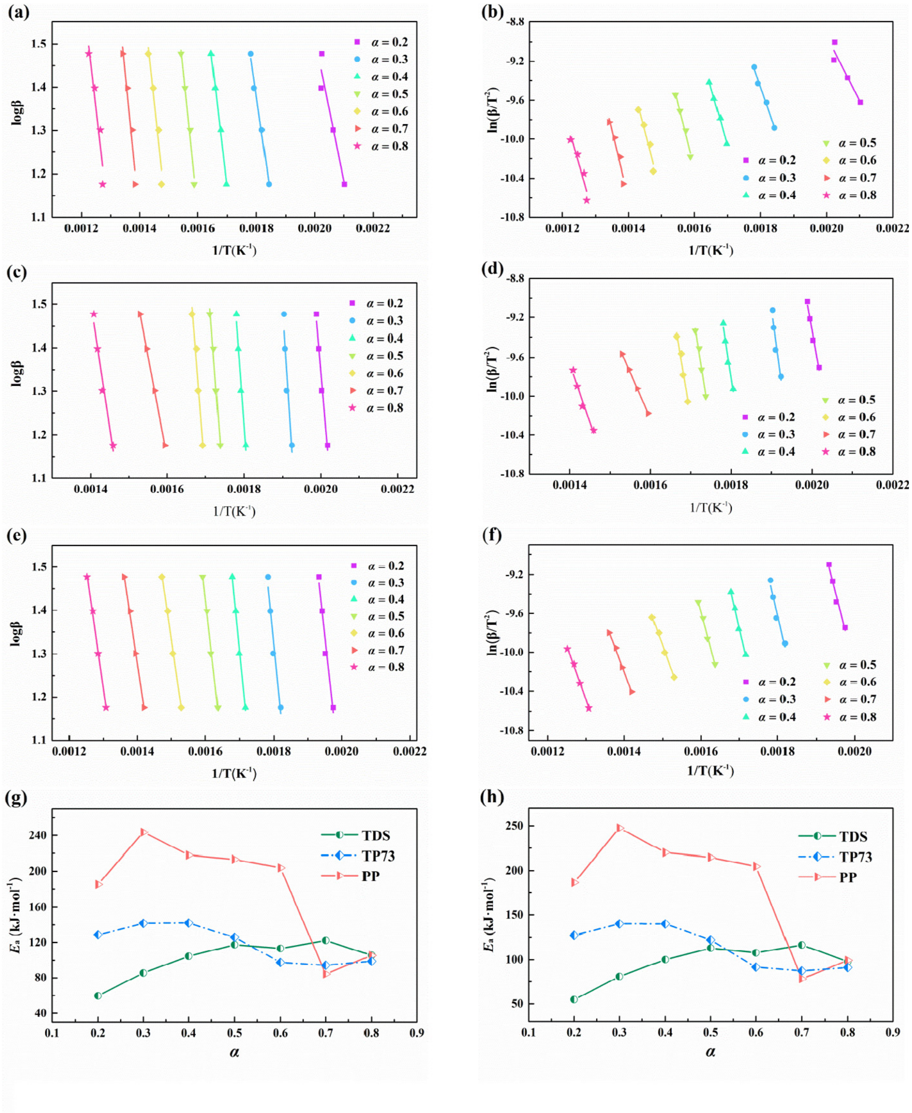

Fig. 6. Plots at different α for: TDS (a) by FWO and (b) KAS; PP (c) by FWO and (d) KAS; TP73 (e) by FWO and (f) KAS; the relationship between E_a and different α determined by (g) FWO and (h) KAS.

although their transmittance peaks were not obvious. The (co-) combustion products discussed above could be observed in the same absorption bands from PP (Fig. 5(d)) and TP73 (Fig. 5(f)).

The evolution tendencies of the gaseous products generated during the (co-)combustion process were presented in the 3-D FTIR spectrograms. In the case of TDS (Fig. 5(a)), the releases of such gases as H_2O, CH_4, CO, CO_2, SO_2, NH_3, and HCN and the mixture of organic products were identified, and their evolution with the increased temperature was observed. These results were in agreement with their previous discussion for the degradation stages of TDS. For example, the release amount of CO_2 was maintained to a large extent between 300 and 700 °C and reached its maximum at 480 °C. Between 300 and 600 °C, the emissions of CH_4 and CO were observed. These behaviors could be associated with the second stage (208–675 °C) of the release of volatile matters. In contrast, the release amount of CO_2 for PP was much greater than that for TDS due to the more decomposition of organic compounds in PP as described above. It should be noted that the releases of H_2O, CO and CO_2 were enhanced significantly between 200 and 600 °C, while NH_3, HCN and a mixture of organics product occurred between 200 and 400 °C. As can be seen in Fig. 5(e), the absorbance of the products from TP73 was much lower than that of the individual samples which revealed trace amounts of CO_2, H_2O and light organics. This might be associated with the interaction between TDS and PP, as analyzed in Section 3.3.

3.7. Kinetic analysis

The kinetic parameters of TDS, PP and TP73 under the heating rates of 15, 20, 25 and 30 $^\circ C \cdot min^{-1}$ calculated by FWO and KAS methods are shown in Fig. 6. The fitted curves of E_a for the samples in a series of conversions ($\alpha = 0.2$ to 0.8) are presented in Fig. 6(a)–(f). R^2 values of E_a ranged from 90.22 to 100%, thus validating the admissible accuracy of our results. The deviations of the E_a estimates according to the FWO and KAS methods were 5.24, 0.22, and 3.63% for TDS, PP, and TP73, respectively. The E_a estimates by the methods presented a similar trend.

The activation energy determines the activity and sensitivity for a chemical reaction, and its variation reveals a multi-stage process during the thermal decomposition corresponding to different conversions. The E_a values for TDS increased rapidly before $\alpha = 0.5$, underwent a small fall, reached the maximum value at $\alpha = 0.7$ and decreased promptly thereafter (Fig. 6(g) and (h)). The E_a values for PP initially increased until $\alpha = 0.3$, decreased slowly before $\alpha = 0.6$, dropped suddenly, reached the minimum value at $\alpha = 0.7$ and finally grew slightly when α varied between 0.7 and 0.8. This was consistent with the tendency of the TG curves. In contrast, the E_a values for TP73 initially increased slightly before $\alpha = 0.3$, decreased and stayed at the lower levels (94.3–98.8 $kJ \cdot mol^{-1}$ for FWO and 87.2–91.5 $kJ \cdot mol^{-1}$ for KAS). When $\alpha = 0.2$ to 0.8, the E_a values were in the range of 59.7–122.2 $kJ \cdot mol^{-1}$ for TDS, 84.4–243.5 $kJ \cdot mol^{-1}$ for PP and 94.3–142.1 $kJ \cdot mol^{-1}$ for TP73 by FWO. This case indicated that the interaction between TDS and PP finally impacted the E_a values of the blends [8,53].

4. Conclusions

The co-combustion characteristics of TDS and PP were studied for the first time using TG-FTIR. With the increased PP ratio, DTG_{max} and S increased, whereas T_i, T_f, T_m and M_f decreased. The interactions between TDS and PP exerted inhibitive effects on the co-combustion process. The results of XRF showed the high alkali metal and alkali earth metal contents of PP and the high aluminosilicate mineral contents of TDS. The alkali metals of PP might react with the minerals of TDS to form low-temperature sticky melts by which the agglomeration and clinkering of TP blends might arise, thus hindering the co-combustion process. The gaseous releases of H_2O, CH_4, CO, CO_2, SO_2, NH_3, and HCN were observed from the FTIR spectrums of the individual samples. In contrast, less emissions of CO_2, H_2O, and light organics were generated from the TP73 co-combustion. The E_a estimates based on the FWO and KAS methods presented similar trends.

Acknowledgements

This work was supported by the Science and Technology Planning Project of Guangdong Province, China (No.2017A050501036; 2015B020235013; 2017A040403045), the Scientific and Technological Planning Project of Guangzhou, China (No.201704030109; 2016201604030058) and Guangdong Special Support Program for Training High Level Talents (No.2014TQ01Z248).

References

[1] Ministry of Environmental Protection (MEP), P. R. China, Annual Statistic Report on Environment in China, China Environmental Science Press, 2013.
[2] A.B. dos Santos, F.J. Cervantes, J.B. van Lier, Review paper on current technologies for decolourisation of textile wastewaters: perspectives for anaerobic biotechnology, Bioresour. Technol. 98 (2007) 2369–2385.
[3] Z. Zhuo, J. Liu, S. Sun, J. Sun, J. Kuo, K. Chang, J. Fu, Y. Wang, Thermogravimetric characteristics of textile dyeing sludge, coal and their blend in N_2/O_2 and CO_2/O_2 atmospheres, Appl. Therm. Eng. 111 (2017) 87–94.
[4] Y. Liao, X. Ma, Thermogravimetric analysis of the co-combustion of coal and paper mill sludge, Appl. Energy 87 (2010) 3526–3532.
[5] N.V. Avelar, A.A.P. Rezende, A.d.C.O. Carneiro, C.M. Silva, Evaluation of briquettes made from textile industry solid waste, Renew. Energy 91 (2016) 417–424.
[6] M. Huang, L. Chen, D. Chen, S. Zhou, Characteristics and aluminum reuse of textile sludge incineration residues after acidification, J. Environ. Sci. 23 (2011) 1999–2004.
[7] A. Kelessidis, A.S. Stasinakis, Comparative study of the methods used for treatment and final disposal of sewage sludge in European countries, Waste Manag. 32 (2012) 1186–1195.
[8] X. Peng, X. Ma, Z. Xu, Thermogravimetric analysis of co-combustion between microalgae and textile dyeing sludge, Bioresour. Technol. 180 (2015) 288–295.
[9] L. Huang, J. Liu, Y. He, S. Sun, J. Chen, J. Sun, K. Chang, J. Kuo, X.a. Ning, Thermodynamics and kinetics parameters of co-combustion between sewage sludge and water hyacinth in CO_2/O_2 atmosphere as biomass to solid biofuel, Bioresour. Technol. 218 (2016) 631–642.
[10] S. Yurdakul, Determination of co-combustion properties and thermal kinetics of poultry litter/coal blends using thermogravimetry, Renew. Energy 89 (2016) 215–223.
[11] V. Dhyani, T. Bhaskar, A comprehensive review on the pyrolysis of lignocellulosic biomass, Renew. Energy 146 (2013) 371–378.
[12] R. Font, A. Fullana, J. Conesa, Kinetic models for the pyrolysis and combustion of two types of sewage sludge, J. Anal. Appl. Pyrol. 74 (1–2) (2005) 429–438.
[13] J. Liu, S. Sun, Comprehensive evaluation of municipal sewage sludge combustion characteristics and its combustion kinetics model in Guangzhou, Huan Jing Ke Xue Xue Bao 32 (2012) 1952–1961.
[14] M.B. Folgueras, R.M. Dıaz, J. Xiberta, I. Prieto, Thermogravimetric analysis of the co-combustion of coal and sewage sludge, Fuel 82 (2003) 2051–2055.
[15] M.V. Kok, E. Özgür, Thermal analysis and kinetics of biomass samples, Fuel Process. Technol. 106 (2013) 739–743.
[16] X. Wang, S. Deng, H. Tan, A. Adeosun, M. Vujanović, F. Yang, N. Duić, Synergetic effect of sewage sludge and biomass co-pyrolysis: a combined study in thermogravimetric analyzer and a fixed bed reactor, Energy Convers. Manag. 118 (2016) 399–405.
[17] S. Deng, X. Wang, H. Tan, H. Mikulčić, F. Yang, Z. Li, N. Duić, Thermogravimetric study on the co-combustion characteristics of oily sludge with plant biomass, Thermochim. Acta 633 (2016) 69–76.
[18] R. Huang, M. Cao, H. Guo, W. Qi, R. Su, Z. He, Enhanced ethanol production from pomelo peel waste by integrated hydrothermal treatment, multienzyme formulation, and fed-batch operation, J. Agric. Food Chem. 62 (2014) 4643–4651.
[19] W. Wang, X. Ma, Y. Xu, Y. Cao, Z. Jiang, T. Ding, X. Ye, D. Liu, Ultrasound-assisted heating extraction of pectin from grapefruit peel: optimization and comparison with the conventional method, Food Chem. 178 (2015) 106–114.
[20] J. He, P. Shao, J. Liu, Q. Ru, Supercritical carbon dioxide extraction of flavonoids from pomelo (citrus grandis (l.) osbeck) peel and their antioxidant activity, Int. J. Mol. Sci. 13 (2012) 13065–13078.
[21] B. Uysal, F. Sozmen, O. Aktas, B.S. Oksal, E.O. Kose, Essential oil composition and antibacterial activity of the grapefruit (Citrus Paradisi. L) peel essential oils obtained by solvent-free microwave extraction: comparison with

hydrodistillation, Int. J. Food Sci. Technol. 46 (2011) 1455–1461.
[22] M.E. Argun, D. Güclü, M. Karatas, Adsorption of Reactive Blue 114 dye by using a new adsorbent: pomelo peel, J. Ind. Eng. Chem. 20 (2014) 1079–1084.
[23] X. Peng, X. Ma, Y. Lin, Z. Guo, S. Hu, X. Ning, Y. Cao, Y. Zhang, Co-pyrolysis between microalgae and textile dyeing sludge by TG–FTIR: kinetics and products, Energy Convers. Manag. 100 (2015) 391–402.
[24] B. Zapata, J. Balmaseda, E. Fregoso-Israel, E. Torres-García, Thermo-kinetics study of orange peel in air, J. Therm. Anal. Calorim. 98 (2009) 309–315.
[25] D. López-González, M. Fernandez-Lopez, J.L. Valverde, L. Sanchez-Silva, Kinetic analysis and thermal characterization of the microalgae combustion process by thermal analysis coupled to mass spectrometry, Appl. Energy 114 (2014) 227–237.
[26] Z. Liu, R. Balasubramanian, A comparison of thermal behaviors of raw biomass, pyrolytic biochar and their blends with lignite, Bioresour. Technol. 146 (2013) 371–378.
[27] A. Agrawal, S. Chakraborty, A kinetic study of pyrolysis and combustion of microalgae Chlorella vulgaris using thermo-gravimetric analysis, Bioresour. Technol. 128 (2013) 72–80.
[28] R. Junga, W. Knauer, P. Niemiec, M. Tańczuk, Experimental tests of co-combustion of laying hens manure with coal by using thermogravimetric analysis, Renew. Energy 111 (2017) 245–255.
[29] J. Naktiyok, H. Bayrakçeken, A.K. Özer, M.Ş. Gülaboğlu, Kinetics of thermal decomposition of phospholipids obtained from phosphate rock, Fuel Process. Technol. 116 (2013) 158–164.
[30] J. Wang, K. Yang, Z. Xu, C. Fu, Energy and exergy analyses of an integrated CCHP system with biomass air gasification, Appl. Energy 142 (2015) 317–327.
[31] R. Miranda, D. Bustos-Martinez, C.S. Blanco, M.H.G. Villarreal, M.E.R. Cantú, Pyrolysis of sweet orange (Citrus sinensis) dry peel, J. Anal. Appl. Pyrol. 86 (2009) 245–251.
[32] N. Chen, J. Ren, Z. Ye, Q. Xu, J. Liu, S. Sun, Kinetics of coffee industrial residue pyrolysis using distributed activation energy model and components separation of bio-oil by sequencing temperature-raising pyrolysis, Bioresour. Technol. 221 (2016) 534–540.
[33] R.K. Mishra, K. Mohanty, Pyrolysis kinetics and thermal behavior of waste sawdust biomass using thermogravimetric analysis, Bioresour. Technol. 251 (2018) 63–74.
[34] O. Francioso, M.T. Rodriguez-Estrada, D. Montecchio, C. Salomoni, A. Caputo, D. Palenzona, Chemical characterization of municipal wastewater sludges produced by two-phase anaerobic digestion for biogas production, J. Hazard. Mater. 175 (2010) 740–746.
[35] H. Yang, R. Yan, H. Chen, C. Zheng, D.H. Lee, D.T. Liang, In-depth investigation of biomass pyrolysis based on three major components: hemicellulose, cellulose and lignin, Energy Fuel. 20 (2006) 388–393.
[36] J.L.L. Gašparovič, J. Markoš, L. Jelemensky, Calculation of kinetic parameters of the thermal decomposition of wood by distributed activation energy model (DAEM), Chem. Biochem. Eng. Q. 26 (2012) 45–53.
[37] Z. Yu, X. Ma, A. Liu, Thermogravimetric analysis of rice and wheat straw catalytic combustion in air- and oxygen-enriched atmospheres, Energy Convers. Manag. 50 (2009) 561–566.
[38] Y. Zhang, Y. Guo, F. Cheng, K. Yan, Y. Cao, Investigation of combustion characteristics and kinetics of coal gangue with different feedstock properties by thermogravimetric analysis, Thermochim. Acta 614 (2015) 137–148.
[39] S. Niu, K. Han, C. Lu, Characteristic of coal combustion in oxygen/carbon dioxide atmosphere and nitric oxide release during this process, Energy Convers. Manag. 52 (2011) 532–537.
[40] M. Mureddu, F. Dessì, A. Orsini, F. Ferrara, A. Pettinau, Air- and oxygen-blown characterization of coal and biomass by thermogravimetric analysis, Fuel 212 (2018) 626–637.
[41] Z. Xie, X. Ma, The thermal behaviour of the co-combustion between paper sludge and rice straw, Bioresour. Technol. 146 (2013) 611–618.
[42] E. Kastanaki, D. Vamvuka, P. Grammelis, E. Kakaras, Thermogravimetric studies of the behavior of lignite–biomass blends during devolatilization, Fuel Process. Technol. 77–78 (2002) 159–166.
[43] X. Liu, M. Chen, D. Yu, Oxygen enriched co-combustion characteristics of herbaceous biomass and bituminous coal, Thermochim. Acta 569 (2013) 17–24.
[44] H.B. Vuthaluru, Thermal behaviour of coal/biomass blends during co-pyrolysis, Fuel Process. Technol. 85 (2004) 141–155.
[45] G. Zheng, J.A. Koziński, Thermal events occurring during the combustion of biomass residue, Fuel 79 (2000) 181–192.
[46] J. Chen, L. Mu, J. Cai, H. Yin, X. Song, A. Li, Thermal characteristics and kinetics of refining and chemicals wastewater, lignite and their blends during combustion, Energy Convers. Manag. 100 (2015) 201–211.
[47] Z. Yao, X. Ma, Z. Wang, L. Chen, Characteristics of co-combustion and kinetic study on hydrochar with oil shale: a thermogravimetric analysis, Appl. Therm. Eng. 110 (2017) 1420–1427.
[48] H.A. Tchapda, V.S. Pisupati, A review of thermal co-conversion of coal and biomass/waste, Energies 7 (2014) 1098–1148.
[49] R. Habibi, J. Kopyscinski, M.S. Masnadi, J. Lam, J.R. Grace, C.A. Mims, J.M. Hill, Co-gasification of biomass and non-biomass feedstocks: synergistic and inhibition effects of switchgrass mixed with sub-bituminous coal and fluid coke during CO_2 gasification, Energy Fuel. 27 (2013) 494–500.
[50] J.M. Oladejo, S. Adegbite, C.H. Pang, H. Liu, A.M. Parvez, T. Wu, A novel index for the study of synergistic effects during the co-processing of coal and biomass, Appl. Energy 188 (2017) 215–225.
[51] J. Yan, X. Jiang, X. Han, J. Liu, A TG–FTIR investigation to the catalytic effect of mineral matrix in oil shale on the pyrolysis and combustion of kerogen, Fuel 104 (2013) 307–317.
[52] T. Ahamad, S.M. Alshehri, TG–FTIR–MS (Evolved Gas Analysis) of bidi tobacco powder during combustion and pyrolysis, J. Hazard. Mater. 199–200 (2012) 200–208.
[53] C. Chen, X. Ma, Y. He, Co-pyrolysis characteristics of microalgae Chlorella vulgaris and coal through TGA, Bioresour. Technol. 117 (2012) 264–273.